

Mechanism of the Hydride Transfer between *Anabaena* Tyr303Ser FNR_{rd}/FNR_{ox} and NADP⁺/H. A Combined Pre-Steady-State Kinetic/Ensemble-Averaged Transition-State Theory with Multidimensional Tunneling Study

Isaias Lans,[†] José Ramón Peregrina,[†] Milagros Medina,[†] Mireia Garcia-Viloca,^{*} Angels González-Lafont,[‡] and José M. Lluch[‡]

Departamento de Bioquímica y Biología Molecular y Celular, Facultad de Ciencias, and Institute of Biocomputation and Physics of Complex Systems (BIFI), Universidad de Zaragoza, E-50009 Zaragoza, Spain, and Departament de Química and Institut de Biotecnologia i de Biomedicina, Universitat Autònoma de Barcelona, 08193 Bellaterra (Barcelona), Spain

Received: December 21, 2009

The flavoenzyme ferredoxin-NADP⁺ reductase (FNR) catalyzes the production of NADPH during photosynthesis. The hydride-transfer reactions between the *Anabaena* mutant Tyr303Ser FNR_{rd}/FNR_{ox} and NADP⁺/H have been studied both experimentally and theoretically. Stopped-flow pre-steady-state kinetic measurements have shown that, in contrast to that observed for WT FNR, the physiological hydride transfer from Tyr303Ser FNR_{rd} to NADP⁺ does not occur. Conversely, the reverse reaction does take place with a rate constant just slightly slower than for WT FNR. This latter process shows temperature-dependent rates, but essentially temperature independent kinetic isotope effects, suggesting the reaction takes place following the vibration-driven tunneling model. In turn, ensemble-averaged variational transition-state theory with multidimensional tunneling calculations provide reaction rate constant values and kinetic isotope effects that agree with the experimental results, the experimental and the theoretical values for the reverse process being noticeably similar. The reaction mechanism behind these hydride transfers has been analyzed. The formation of a close contact ionic pair FADH[−]:NADP⁺ surrounded by the polar environment of the enzyme in the reactant complex of the mutant might be the cause of the huge difference between the direct and the reverse reaction.

1. Introduction

The flavoenzyme ferredoxin-NADP⁺ reductase (FNR) catalyzes the electron transfer from ferredoxin (Fd) to the nicotinamide adenine dinucleotide phosphate (NADP⁺) to produce NADPH in photosynthesis.^{1–5} Beyond this photosynthetic role in chloroplasts and cyanobacteria vegetative cells, flavoproteins with FNR activity are ubiquitous among living organisms, having been reported, for instance, in phototrophic and heterotrophic bacteria, animal and yeast mitochondria, and apicoplasts.^{3,6,7} The FNR structure consists of two distinct domains.^{8–10} The N-terminal domain forms the binding site of the flavin adenine dinucleotide (FAD) redox cofactor, whereas the C-terminal domain binds the NADP⁺ coenzyme. The global reversible two-electron transfer from Fd to NADP⁺ requires the formation of a transient ternary complex Fd:FNR:NADP⁺, in which oxidized FNR (FNR_{ox}) forms a complex with NADP⁺ prior to its association with reduced Fd (Fd_{rd}). Once the FNR is reduced to its anionic hydroquinone state (FNR_{rd}), by two sequential electron transfers from two independent Fd_{rd} molecules, the anionic reduced isoalloxazine ring of its FAD cofactor (FADH[−]) and the oxidized nicotinamide ring of the NADP⁺ coenzyme must be placed in a relative orientation that makes possible a functional hydride transfer from the N₅ of the flavin isoalloxazine to the C₄N of the nicotinamide ring of the coenzyme (Figure 1).^{2,5,11–13}

Different X-ray structures of the *Anabaena* FNR:NADP⁺ complex envisage a mechanism for the enzyme:coenzyme

interaction and for the approximation between the isoalloxazine and nicotinamide rings.¹⁰ The first stage would be the recognition of the 2′P-AMP moiety of NADP⁺ by FNR.⁹ Then, a narrowing of the FNR coenzyme binding cavity is proposed to fit the 2′P-AMP and pyrophosphate, addressing the nicotinamide toward the FAD cofactor.^{2,10} In this complex Tyr303 stacks against the isoalloxazine ring (as also observed in the free enzyme), leaving the C₄N atom so far from the flavin N₅ atom as 7.78 Å. Therefore, it is proposed that the isoalloxazine:Tyr303 stacking has to be disrupted, and this tyrosine has to be displaced to allow the entrance of the nicotinamide into the active site. However, the final architecture and relative orientation of the isoalloxazine, nicotinamide, and Tyr rings in the active site of the catalytically competent complex are far to be known.^{14,15}

Several FNR variants from *Anabaena* and pea in which the C-terminal Tyr303 (Tyr308 in pea) has been replaced by Trp, Phe, or Ser have been produced.^{14,16} The crystal structures of the complexes of the Ser mutants with NADP⁺ show how the nicotinamide and the isoalloxazine rings are close to each other.^{14,17} In the *Anabaena* complex (Figure 1), the C₄N and the N₅ are 3.4 Å apart, close enough to make the hydride transfer an available process. The nicotinamide and the isoalloxazine rings are aligned with an angle of roughly 30°: the C₄N atom is the closest to the isoalloxazine ring, and the N₁N atom the farthest (4.6 Å from the flavin N₁₀ atom).

Pre-steady-state studies of the hydride transfer between *Anabaena* wild type (WT) FNR and NADP⁺/H confirmed that two different charge-transfer complexes (CTCs) are formed prior and upon hydride transfer,¹⁸ as previously shown by higher plant FNRs.¹¹ In the physiological reaction of FNR_{rd} with NADP⁺,

* Corresponding author. E-mail: mireia@bioinf.uab.es.

[†] Universidad de Zaragoza.

[‡] Universitat Autònoma de Barcelona.

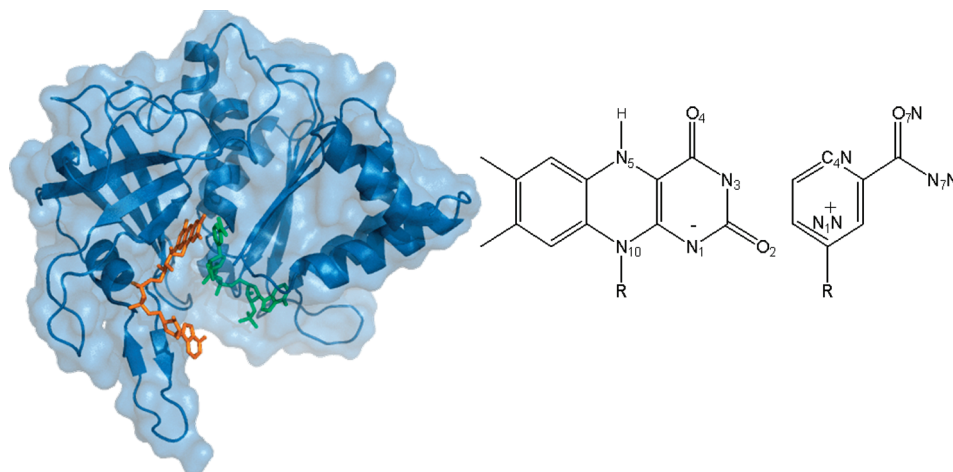


Figure 1. Cartoon and surface representation of the crystal structure of the *Anabaena* Tyr303Ser FNR:NADP⁺ complex (pdb code 2bsa). The FAD cofactor and the NADP⁺ coenzyme are shown in sticks and colored in orange and green, respectively. The number of the most relevant atoms of the isoalloxazine ring of FAD and the nicotinamide ring of NADP⁺ is also shown.

formation of the FNR_{rd}-NADP⁺ CTC (labeled as CTC-2), as well as part of the hydride-transfer reaction (herein referred to as HT-1), took place within the experimental measurement dead time. At the equilibrium point despite full FNR reoxidation was not achieved, detectable amounts of the FNR_{ox}-NADPH (CTC-1) complex were found, while CTC-2 accumulated to a small extent and quickly evolved. That is, the equilibrium mixture is displaced toward NADPH production (Figure S1, Supporting Information), consistent with the physiological main role of FNR. These facts were confirmed when analyzing the reverse reaction (hydride transfer herein referred to as HT). In contrast, reduction of pea Tyr308Ser FNR_{ox} in the presence of NADP⁺ leads to the formation of an appreciable amount of the CTC-2, instead of the CTC-1.¹⁷ Then it is evident that the behavior of the pea Tyr308Ser FNR is opposite to the one corresponding to the *Anabaena* WT FNR, although it is not clear why. Note that, although the C-terminal Tyr is assumed not to be indispensable for the hydride transfer, its substitution by a Ser practically deactivates the capacity of the enzyme to reduce NADP⁺, despite the apparent favorable structural disposition in the mutant between the nicotinamide and the isoalloxazine rings to produce the hydride transfer.^{14,16,17}

In this context, we present here two complementary studies of the hydride-transfer processes between *Anabaena* Tyr303Ser FNR_{rd}/FNR_{ox} and NADP⁺/H: First, an experimental pre-steady-state kinetic study; second, a theoretical study based on the ensemble-averaged transition-state theory with multidimensional tunneling. These studies enable us a better understanding of how FNR works and shed light on the role of the C-terminal Tyr, while we wait for a structural model that represents the catalytically competent complex in the WT to carry out the corresponding theoretical study.

2. Materials and Experimental Methods

2.1. Biological Materials and Chemicals. *Anabaena* WT and Tyr303Ser FNR were produced as previously reported.¹⁹ Reduced FNRs were obtained by photoreduction in the presence of 3 mM EDTA and 2–5 μ M 5-deazariboflavin in 50 mM Tris/HCl, pH 8.0.^{18,20} Deuterated FNR_{rd} (D-FNR_{rd}) variants were produced by photoreduction of FNR_{ox} previously dialyzed in 50 mM Tris/DCl, pD \sim 8.0 in D₂O. NADPD (4R-form, with the deuterium in the A face of the nicotinamide) was produced and purified as described.²¹ Chemicals were from Sigma-Aldrich.

2.2. Stopped-Flow Pre-Steady-State Kinetic Measurements.

Fast CTC formation and hydride (or deuteride) transfer between NADPH (or NADPD) and FNR_{ox} or FNR_{rd} (or D-FNR_{rd}) and NADP⁺ were studied by stopped-flow methodology in 50 mM Tris/HCl, pH 8.0 (or pD 8.0 for deuteride-transfer measurements) at 279 K under anaerobic conditions.^{13,18} Final FNR concentrations were 25 μ M, while a 25–250 μ M range was used for the coenzymes. Reactions were analyzed by following the evolution of the absorption spectra (400–1000 nm) using an Applied Photophysics SX17.MV stopped-flow with a photodiode array detector. Multiple wavelength absorption data were collected and processed using the X-Scan software (App. Photo. Ltd.). A total of 400 spectra per second were collected. Time spectral deconvolution was performed by global analysis and numerical integration methods using Pro-Kineticist (App. Photo. Ltd.). Data were best fit to a single step, B \rightarrow C, model that allowed estimation of the conversion rate constants ($k_{B \rightarrow C}$) as previously reported.¹⁸ In all the analyzed cases a previous reaction had occurred in the instrumental dead time (A \rightarrow B). The determined species B and C are spectral species, reflecting a distribution of enzyme intermediates at a certain point along the reaction time course, and do not necessarily represent a single distinct enzyme intermediate. Model validity was assessed by lack of systematic deviations from residual plots at different wavelengths, inspection of calculated spectra, and consistence among the number of significant singular values with the fit model. Simulations using Pro-Kineticist were also performed to validate the results, the determined hydride-transfer kinetics constants for the physiological (k_{HT-1}) and reverse (k_{HT}) (or k_{DT-1} , k_{DT} for the corresponding deuteride transfers) processes and the mechanism.¹⁸ For accurate estimation of temperature dependence of hydride- and deuteride-transfer rate constants, single-wavelength kinetic traces were recorded at 458 nm and different temperatures between 278.35 and 290.35 K, and saturating coenzyme concentrations using the SX18.MV software (App. Photo. Ltd.). These traces were fit into a standard monoexponential decay to determine the observed conversion rate constants (k_{obs}) under saturating coenzyme concentrations. Errors in the determination of kinetic rate constants were \pm 15%.

3. Computational Details

In the present study we have used the well-known QM/MM (quantum mechanics/molecular mechanics) methodology,^{22–24}

which allows the simulation of reactions in large molecular systems by means of the partition of the system into a QM part, where the reaction occurs, and a MM part, which perturbs the QM region through electrostatic and van der Waals interactions.

3.1. Gas-Phase Calculations. The QM method employed in the enzymatic QM/MM calculations is the semiempirical Austin Model 1 (AM1).²⁵ To investigate the performance of the AM1 calculations for the biological system studied, we performed gas-phase calculations on a model system, which represents the interaction between the reactant species. Specifically, a lumiflavin molecule and a 1-methylnicotinamide molecule have been used to model the isoalloxazine and nicotinamide rings of the FADH[−]/FAD cofactor and NADP⁺/NADPH coenzyme, respectively. The Gaussian03²⁶ package has been used to carry out these calculations.

The energy of reaction and barrier height for the hydride transfer between these two model compounds have been determined at the semiempirical AM1 level and at the MPWB1K²⁷ density functional level using the split valence 6-31+G(d,p) basis set. Full geometry optimization and direct location of stationary points have been done with the Schlegel gradient optimization algorithm at the two levels of calculation. The characterization of both kinds of stationary points, minima, or transition-state structures, has been carried out by diagonalizing their Hessian matrices and looking for zero or one negative eigenvalue, respectively.

In addition, complexation energies for the localized reactant and product complexes have been calculated at the semiempirical AM1 level, and with the B3LYP^{28,29} and MPWB1K density functionals with the 6-31+G(d,p) basis set.

3.2. Model of the Biological System. In this work the Cartesian coordinates in the file with PDB code 2BSA have been used to build a model of the Michaelis complex between the mutant Tyr303Ser FNR and NADP⁺. This crystallographic structure contains 295 residues, 279 crystallographic waters, the prosthetic group (FAD), and the coenzyme (NADP⁺). The oxidized FAD cofactor was replaced by FADH[−] to simulate the hydride transfer from FADH[−] to NADP⁺.

The coordinates for the hydrogen atoms of the protein and the coenzyme were determined using the HBUILD facility in the program CHARMM.³⁰ To determine the protonation states of all ionizable residues, we calculated the pK_a's of each of them in the Tyr303Ser FNR mutant at pH 7.0 using the PROPKA^{31,32} module of the PDB2PQR^{33,34} software package. The net charge of the system after protonation was −7 e, which was neutralized with 7 sodium cations. The final protein structure was solvated with a previously equilibrated cubic box of water molecules, centered at the geometric center of the protein complex. The initial dimensions of the box were 83 Å × 75 Å × 63 Å, which ensures that all protein atoms are at least 16 Å away from the edges of the box. Water molecules that are within 2.0 Å of any non-hydrogen atoms of the protein or ligand were removed. The final model contains 41 896 atoms, of which 4800 are protein atoms.

3.3. Potential Energy Surface. To equilibrate the solvated protein system, we first carried out molecular dynamics (MD) simulations using the all-atom CHARMM22 force field³⁵ to represent the protein, the FADH[−], and the NADP⁺ molecules. The three-point-charge TIP3P^{35,36} model was used for water. The parameters for the FADH[−] molecule were derived from standard CHARMM22 parameters of analogous compounds, with the exception of the charges, which were obtained following the RESP^{37,38} fitting of point charges procedure. We

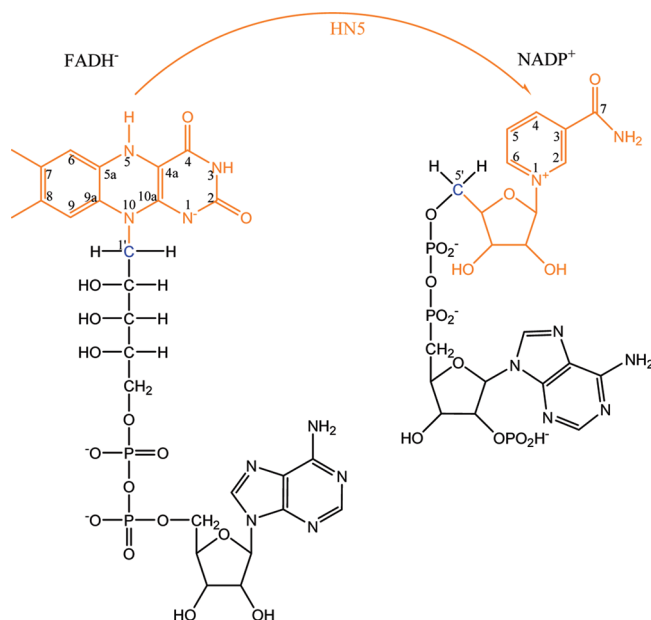


Figure 2. Definition of the QM region (atoms in orange) used for the QM/MM calculations. The boundary atoms are marked in blue.

note that these parameters were used only for the purpose of initial equilibration of the system.

For combined QM/MM calculations, the system was partitioned into a quantum mechanical region consisting of 58 atoms and a molecular mechanical region containing the rest of the system. The QM system is shown in Figure 2 and includes the triple ring of flavin of the cofactor (FADH[−]), and the nicotinamide and ribose rings of the coenzyme (NADP⁺/H). The QM subsystem contains two boundary atoms (see Figure 2): the C1' atom attached to the N₁₀ atom of the flavin ring, and the C5' ribose atom, which are represented by the GHO method.²⁴

The QM subsystem was described with the AM1 semiempirical Hamiltonian. We used a single-point dual-level scheme to correct AM1 potential energies with respect to the MPWB1K hybrid density functional results on geometries of a subset of QM atoms (QM-c) along the hydride-transfer energy profile generated with the whole QM/MM model. More details about this procedure are given in the Theoretical Results section.

3.4. Simulations. All the simulations were done at 279 K.

3.4.1. Classical Molecular Dynamics of the Reactant. To remove close contacts and highly repulsive orientations of the initial protein–solvent system, we first performed 100 steps of energy minimization for all water molecules using the adopted-basis Newton–Raphson (ABNR) method in the program CHARMM,³⁰ with the protein atoms held fixed. This was followed by 100 steps of restrained energy minimization of the entire system. The restraints were harmonic potentials applied to the heavy atoms of the cofactor, coenzyme, and protein backbone atoms. Harmonic constants of 50 and 20 kcal/(mol Å²) were used for the cofactor and the coenzyme atoms and for the protein atoms, respectively. From the resulting configuration, MD simulations with periodic boundary conditions (PBC) in a isothermal–isobaric (NPT) ensemble at 279 K and 1 atm were carried out. A spherical cutoff of 13 Å for the nonbonded interactions has been applied together with a switching function acting between 12.5 and 11.5 Å. The nonbonded pair list was updated every 25 steps. The particle mesh Ewald method³⁹ with a grid spacing of 1 Å has been used. We used the leapfrog algorithm⁴⁰ to propagate the equations of motion with a time step of 2 fs. All bond length and bond angles

involving hydrogen atoms were constrained by the SHAKE algorithm,⁴¹ and the dielectric constant was set to 1.

Initially, the temperature of the system was gradually raised from 0 to 279 K in 32 ps under the harmonic restraints described above for the minimizations. Then, the system was equilibrated for 90 ps, maintaining the restraints on FADH⁻, but gradually releasing the ones on the coenzyme, and with all protein atoms free to move. From this point, all the following simulations were carried out on the QM/MM potential energy surface described in the previous subsection.

3.4.2. QM/MM Potential Energy Profile. From the final MM equilibrated structure, a 1-D QM/MM potential energy profile for the hydride-transfer process was calculated along the distinguished reaction coordinate z defined in the Theoretical Results section and with all the atoms 20 Å away from the center of the active site kept frozen. The 1-D profile was obtained by a series of geometry optimizations of the mobile part of the system in the presence of harmonic restraints applied on the reaction coordinate. The RESD module in CHARMM³⁰ was used with a restraining force constant of 2500.0 kcal/(mol Å²). Each minimization was carried out with a gradient tolerance of 0.01 kcal/(mol Å) with the ABNR algorithm. In these minimizations the reaction coordinate was projected out of the gradient.

3.4.3. Dynamics. Rate Constants and Kinetic Isotopic Effects. From the same initial structure used to determine the 1-D potential energy profile, QM/MM MD simulations without restrictions were carried out using PBC and the same conditions described in the section 3.4.1 for the MM MD simulations. First, the system was equilibrated for 20 ps to adjust to the changes derived from the new definition of the system as a hybrid QM/MM system. Second, the potential of mean force (PMF) $W^{\text{CM}}(z)$ was determined using the umbrella sampling technique^{42–44} along the reaction coordinate z . A total of 18 separate simulations (or windows) were executed to span the entire range of the reaction coordinate from reactants to products. Each window was equilibrated for 6 ps, and the velocity and positions of the last configuration generated in the previous window were used to initiate the next window. Subsequently, 200 ps were carried out for each window and the probability density of configurations along z was collected and sorted into bins of width 0.01 Å. During the umbrella sampling simulations, the trajectory was saved every 100 steps. The classical PMF was obtained with the weighted histogram analysis method (WHAM).^{42–44}

In the subsequent simulations, we used structural information from the PMF calculations to estimate the rate constant and KIEs of the hydride-transfer reaction from FADH⁻ to NADP⁺, by using the CHARMMRATE⁴⁵ module of CHARMM. We investigated two different systems to determine the primary KIE: the flavin ring with a protium atom attached to the N5 atom and the replacement of protium by deuterium at this position.

The classical mechanical (CM) activation free energy profile is obtained from the CM PMF by⁴⁶

$$\Delta G_{\text{act}}^{\text{CM}}(z) = W^{\text{CM}}(z) - [W^{\text{CM}}(z_{\text{R}}) + G_{\text{R,T,F}}^{\text{CM}}] \quad (1)$$

where z_{R} is the value of z at the reactant (R) minimum of $W^{\text{CM}}(z)$, and $G_{\text{R,T,F}}^{\text{CM}}$ is the CM free energy of the normal mode (F) that corresponds to z at z_{R} . In general, we choose the zero of energy of $W^{\text{CM}}(z)$ so that $W^{\text{CM}}(z_{\text{R}}) = 0$. The CM free energy barrier is $\Delta G_{\text{act}}^{\text{CM}}(z_{\text{M}}^{\text{CM}})$, where z_{M}^{CM} is the value of the reaction coordinate corresponding to the maximum of $W^{\text{CM}}(z)$.

The quantal vibrational correction, $\Delta W_{\text{vib}}(z)$, to the computed PMF was obtained from instantaneous normal-mode analysis,

as described elsewhere.^{46,47} The instantaneous normal-mode frequencies were calculated for 35 atoms that define the primary zone system. This is a subset of the QM region shown in Figure 2 excluding the methyl groups of the flavin ring and the ribose ring. A total of 8500 configurations along the whole reaction coordinate range were used for the calculation of $\Delta W_{\text{vib}}(z)$. When generalized normal-mode frequencies were calculated, the reaction coordinate was projected out of the Hessian, as described in refs 46 and 47. The calculated frequencies for the various configurations were averaged over all the configurations that belong to a given bin of width 0.01 Å, and $\Delta W_{\text{vib}}(z)$ was calculated at different bins.^{46–48} The discrete values were fitted to a continuous Gaussian function. Then, the quasiclassical PMF, $W^{\text{QC}}(z)$ which contains quantized vibrations for the primary zone atoms except for the degree of freedom corresponding to z , is obtained by

$$W^{\text{QC}}(z) = W^{\text{CM}}(z) + \Delta W_{\text{vib}}(z) \quad (2)$$

The quasiclassical activation free energy profile $\Delta G_{\text{act}}^{\text{QC}}$ ⁴⁶ is obtained by

$$\Delta G_{\text{act}}^{\text{QC}}(z) = W^{\text{QC}}(z) - [W^{\text{CM}}(z_{\text{R}}) + G_{\text{R,T,F}}^{\text{CM}} + \Delta W_{\text{vib,R}}] \quad (3)$$

where $\Delta W_{\text{vib,R}}$ is the value of the quantal vibrational correction at the reactant, including both the reaction coordinate and the vibrational modes orthogonal to it. The quasiclassical free energy barrier is $\Delta G_{\text{act}}^{\text{QC}}(z_{\text{M}}^{\text{QC}})$, where z_{M}^{QC} is the value of the reaction coordinate corresponding to the maximum of $W^{\text{QC}}(z)$.

The next step was the calculation of the transmission coefficient in the static secondary zone (SSZ) approximation and using a primary zone somewhat larger than the one used in the calculation of $\Delta W_{\text{vib}}(z)$. In particular, the methyl groups of the flavin ring were now allowed to move. The transition-state ensemble was taken as 8 chosen configurations, which belonged to the z_{M}^{QC} bin. For each of them the minimum energy path (MEP) as a function of the arc length reaction coordinate, s , was calculated as described elsewhere.^{49–51} From these individual reaction paths the net transmission coefficient γ_i is obtained as the product of two factors:^{46,48} the quasiclassical transmission factor, Γ_i , which corrects the rate constant for dynamical recrossing, and the semiclassical transmission coefficient, κ_i , that accounts mainly for tunneling and was calculated with the small-curvature tunneling approximation.⁵² Finally, the average net transmission coefficient is

$$\gamma = \langle \Gamma_i \kappa_i \rangle \quad (4)$$

which gives the final value of the rate constant determined with the ensemble average variational transition-state theory with multidimensional tunneling (EA-VTST/MT)^{46,53} method:

$$k^{\text{EA-VTST/MT}}(T) = \gamma \frac{k_{\text{B}}T}{h} \exp\left(-\frac{\Delta G_{\text{act}}^{\text{QC}}(z_{\text{M}}^{\text{QC}})}{RT}\right) \quad (5)$$

The final theoretical estimate of the phenomenological free energy of activation is

$$\Delta G_{\text{act}}^{\text{EA-VTST/MT}} = \Delta G_{\text{act}}^{\text{QC}}(z_{\text{M}}^{\text{QC}}) - RT \ln \gamma \quad (6)$$

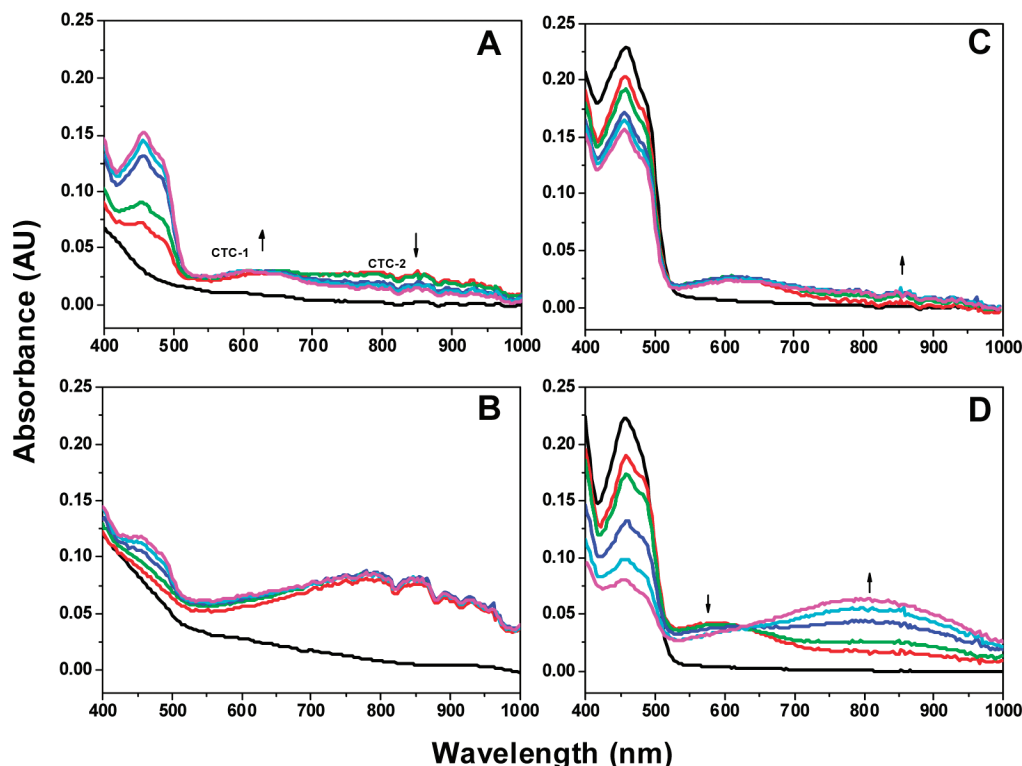


Figure 3. Evolution of spectral changes accompanying the hydride-transfer reactions of WT and Tyr303Ser FNRs with NADP^+/H at 279 K. (A) Time course for the reaction of oxidation of 25 μM WT FNR_{rd} by 125 μM NADP^+ . Spectra recorded at 0.00128, 0.00384, 0.0064, 0.00896, and 0.2547 s. (B) Time course for the reaction of oxidation of 25 μM Tyr303Ser FNR_{rd} by 125 μM NADP^+ . Spectra recorded at 0.00128, 0.00384, 0.0064, 0.01408, and 0.2547 s. (C) Time course for the reaction of reduction of 25 μM WT FNR_{ox} by 125 μM NADPH. Spectra recorded at 0.00128, 0.00384, 0.0064, 0.00896, and 0.2547 s. (D) Time course for the reaction of reduction of 25 μM Tyr303Ser FNR_{ox} by 125 μM NADPH. Spectra recorded at 0.00128, 0.00384, 0.0064, 0.01152, and 0.2547 s. In all cases the black line corresponds to the protein spectrum before mixing with the nucleotide, the red line is the first spectrum after mixing (0.00128 s), and the green, dark blue, light blue, and pink lines correspond to the subsequent ones at the indicated times. Direction of absorbance changes at particular wavelengths are indicated by arrows.

4. Experimental Results

4.1. Intermediate Species during Hydride Transfer between Tyr303Ser FNR and NADP^+/H . Reduction of NADP^+ by Tyr303Ser FNR_{rd} showed the formation of a broad band centered around 800 nm and just partial reoxidation of the flavin band-I (458 nm) within dead time, as reported in WT (Figure 3A,B). This species suggested the presence of a $\text{FNR}_{\text{rd}}\text{-NADP}^+$ CTC (CTC-2, max 798 nm), where the hydride to be transferred is located in the FADH^- -hydride donor.^{18,54} The overall CTC-2 formation event was very fast (impossible to determine $k_{\text{A} \rightarrow \text{B}}$). However, despite showing a fast stabilization of an important amount of CTC-2 the process with Tyr303Ser FNR hardly evolved; conversion to CTC-1 was not observed and only traces of FNR_{ox} were produced (Figure 3B). Such behavior is different from that observed with the WT protein (Figure 3A), where CTC-2 evolves to CTC-1 (580 nm) with the production of NADPH and FNR_{ox} .

When the reverse reaction was followed, FNR_{ox} with NADPH, both WT and Tyr303Ser showed a decrease in the flavin band-I and the appearance of a long-wavelength absorbance band with a maximum around 610 nm within the experimental dead-time (again impossible to determine, $k_{\text{A} \rightarrow \text{B}}$) (Figure 3C,D). The observed long-wavelength band is attributed to a $\text{FNR}_{\text{ox}}\text{:NADPH}$ CTC interaction between the oxidized isoalloxazine and the reduced nicotinamide rings, that is, CTC-1.^{18,54,55} Subsequent evolution of spectra indicated the formation of CTC-2, for both FNR variants (Figure 3C,D).¹⁸

4.2. Hydride-Transfer Efficiency of the FNR Variants. Global analysis of the data obtained at different coenzyme concentrations indicated that all the studied processes best fit a

single step mechanism, corresponding to the evolution of an initial CTC species already produced in the instrumental dead time. These data provided a set of apparent rate constants, $k_{\text{B} \rightarrow \text{C}}$, at different NADP^+/H concentrations, which were independent of the enzyme concentration and could be related with the hydride-transfer rate constant minimal values, $k_{\text{HT-1}}$ or k_{HT} , for the physiological and reverse reactions, respectively. They were in agreement with those determined when considering that, under our experimental conditions and due to the high affinity for the coenzyme (K_{d} values are 5.7 and $<0.01 \mu\text{M}$ for the $\text{FNR}_{\text{ox}}\text{:NADP}^+$ interactions of WT and Tyr303Ser FNRs, respectively¹⁴), the amount of free FNR was lower than that of the free coenzyme.¹⁸ The obtained data indicate that, in contrast to what was observed for WT FNR ($k_{\text{HT-1}}$ of 285 s^{-1}) (Figure 3A), hydride transfer from Tyr303Ser FNR_{rd} to NADP^+ hardly occurred, $k_{\text{HT-1}} \sim 0$, and CTC-2 was highly stabilized. However, traces of FNR_{ox} were produced (Figure 3B). This FNR reoxidation might be a side effect produced by the excess of unbound coenzyme. Its nicotinamide moiety might freely diffuse in solution into the active site and establish a dynamic equilibrium mimicking Tyr303 in WT FNR and reversing the effect of the mutation. In a similar manner, recovery of catalytic efficiency has been reported for the pea Y308S FNR mutant when aromatic compounds are added to the reaction mixture.¹⁵

Hydride transfer from NADPH to Tyr303Ser FNR_{ox} occurred with a k_{HT} of 190 s^{-1} , only slightly slower than for WT (k_{HT} of 270 s^{-1}),¹⁸ but the process was displaced toward the production of FNR_{rd} forms (either CTC-2 or free FNR_{rd}) (Figure 3D). Therefore, a different scheme for the reaction mechanism and equilibrium applies for the mutant with regard to WT (Figure

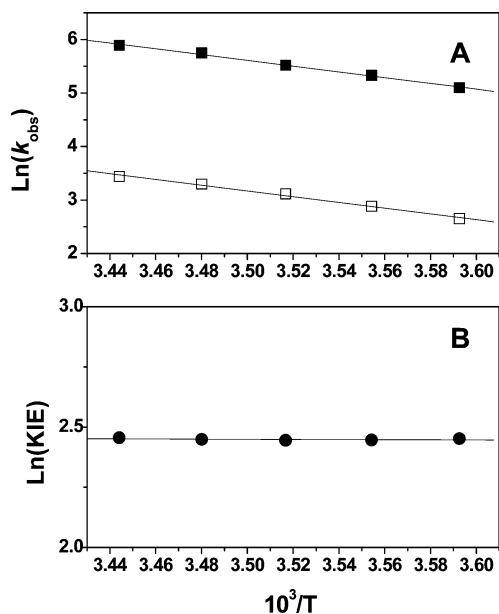


Figure 4. (A) Arrhenius plot of kinetic data for the reduction of Y303S FNR_{ox} by NADPH (closed squares) and by NADPD (open squares). Fits to the Arrhenius equation are shown as solid lines. (B) Temperature dependence of the KIE.

S1, Supporting Information), making the mutant unable to catalyze the physiological reaction. That is, the hydride transfer from NADPH to Tyr303Ser FNR_{ox} is only slightly slower than in the WT enzyme, while the reverse process is undetectable.

4.3. Temperature Dependence of the Hydride-Transfer Reaction of Tyr303Ser FNR and of the Kinetic Isotope Effect. Deuteride-transfer processes were similarly analyzed for Tyr303Ser FNR at 279 K. The overall spectral evolutions were similar to those above-described with the protiated samples; the initial interaction processes were also produced in the instrumental dead time and no deuteride transfer was observed for the reaction of D-FNR_{rd} with NADP⁺. The main observable difference was a considerable decrease in the k_{DT} for the deuteride transfer from NADPD to FNR_{ox} up to 20 s⁻¹, thus producing a kinetic isotopic effect (KIE) of ~ 10 .

The temperature dependence of this last reaction was characterized between 278.35 and 290.35 K for reduction of Tyr303Ser FNR_{ox} both by NADPH and by NADPD. The individual reaction rates are highly dependent on temperature, with important activation energies: 10.73 and 10.68 kcal/mol for the H and D cases, respectively. These values correspond to two practically parallel straight lines in the Arrhenius plot (see Figure 4A). The results, however, show a clear temperature-independent H/D KIE (11.6) within the range of temperatures analyzed (see Figure 4B).

The Arrhenius preexponential factors determined from the intercepts of the plots in Figure 4A turn out to be $A_{\text{H}} = 4.40 \times 10^{10}$ and $A_{\text{D}} = 3.51 \times 10^9$ s⁻¹. Their ratio (12.51) almost matches the value of the KIE, although it is slightly greater due to the practically negligible difference between the two activation energies (0.05 kcal/mol). These features of the KIE indicate that both isotopes tunnel very significantly, although they are not compatible with a rigid, static potential energy barrier, but rather with a fluctuating potential energy barrier that brings the hydride donor and acceptor close together as the temperature increases.^{56,57} Then, this kinetic behavior (essentially temperature independent KIEs, but temperature-dependent rates) has been rationalized in the frame of the vibration-driven tunneling model. Our

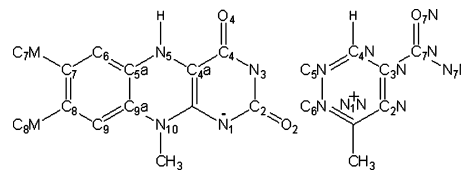


Figure 5. Scheme of the gas-phase model QM-c. For the sake of simplicity some of the hydrogen atoms have not been depicted.

theoretical results (see section 5.5) confirm the relevant role of tunneling in this reaction.

5. Theoretical Results

5.1. Gas-Phase Calculations. As explained in the Computational Details, we have used the AM1 semiempirical method to describe the set of QM atoms of the entire solvated protein system according to the selected QM/MM partition. However, it is well-known that semiempirical methods fail to describe the stabilization contribution of stacking interactions in π -systems because the dispersion contribution to the total interaction energy is not taken into account.^{58,59} On the other hand, broad application of DFT methods to biological systems has also been limited by their inaccurate treatment of dispersion energy. For this reason, an enormous amount of activity has been devoted to the improvement of DFT methods in the last years.^{58–62} In this direction, Zhao and Truhlar have tested their kinetics-optimized functionals on several large dispersion-bonded complexes with reasonable success.^{63,64} In particular, the MPWB1K hybrid functional has been shown to give mean unsigned errors in the complexation energies of DNA base pairs and amino acid pairs nearly 3 times smaller than the well-established and most popular DFT method, B3LYP, that fails badly for dispersion interactions.⁶⁵ In addition, the MPWB1K functional has also been shown to give good results for thermochemical kinetics and hydrogen bonding.^{27,66} For this reason, we selected the MPWB1K hybrid functional as the high-level electronic structure method that will be used to improve the accuracy of the AM1 energies.

Gas-phase calculations of the hydride-transfer reaction between the lumiflavin molecule and 1-methylnicotinamide (see Figure 5), taken as gas-phase models for FADH⁻/FAD and NADP⁺/H, respectively, were carried out. The details of those calculations are included in the Supporting Information. The main conclusion of our gas-phase study of the hydride-transfer reaction confirms the better performance of the MPWB1K hybrid functional. In fact, the energetic difference between B3LYP and MPWB1K complexation energies for the reactant and product complexes found along the hydride-transfer pathway (see Table S2, Supporting Information) has also been reported for other stacked dimers.⁶⁵ So then, the extra stabilization of those two complexes by around 6 kcal/mol at the MPWB1K level can be interpreted as the quantitative correction included by MPWB1K with respect to B3LYP for the stacking contribution to the binding between lumiflavin and 1-methylnicotinamide in gas phase.

In what concerns the hydride-transfer process, it can be observed from the figures in Table S2 (Supporting Information) that at the semiempirical level the reaction is clearly exoergic. This exoergicity is reduced around 10–12 kcal/mol at the B3LYP and the MPWB1K levels, respectively. In turn, the AM1 potential energy barrier for the HT-1 reaction is 3.6 kcal/mol higher than the MPWB1K estimation, but the semiempirical HT potential energy barrier is overestimated by 15.8 kcal/mol in comparison with the MPWB1K result.

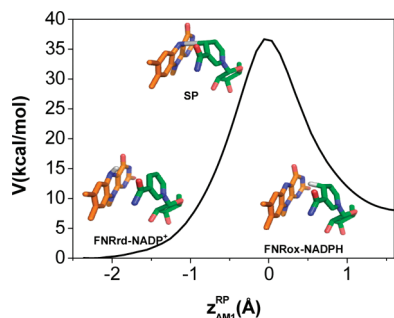


Figure 6. AM1/MM potential energy profiles as a function of z_{AM1}^{RP} .

5.2. Potential Energy Profiles. The first stage consists in the calculation of a 1-D potential energy profile for the hydride-transfer process from [Tyr303Ser FNR_{rd}-NADP⁺] to [Tyr303Ser FNR_{ox}-NADPH] on the QM/MM potential energy surface of the complete solvated system (enzyme/cofactor/coenzyme) along the reaction coordinate z_{AM1}^{RP} , which is defined geometrically as the difference between the N₅-H distance that breaks and the H-C₄N distance that forms. The AM1/MM potential energy profile is depicted in Figure 6 as a function of z_{AM1}^{RP} .

The structures corresponding to the reactant, transition state, and product are located at the values of $z_{AM1}^{RP} = -2.26$ Å, $z_{AM1}^{RP} = -0.06$ Å, and $z_{AM1}^{RP} = 1.74$ Å, respectively. It has to be remarked that the enzyme environment has two relevant effects on the hydride-transfer process in comparison to the situation in gas phase. On one hand, it can be observed that the hydride transfer HT-1 results in an endoergic process (7.8 kcal/mol) in the complete solvated enzymatic system, in contrast with the exoergic AM1 gas-phase hydride-transfer process mentioned in the previous section. The solvated enzyme environment preferentially stabilizes the FNR_{rd}-NADP⁺ complex in contrast to the energy penalty paid in the gas phase by that intermolecular charge separation. The potential energy difference between the transition-state structure and the reactant structure is 36.68 kcal/mol, whereas this difference between the transition-state and product structures is 28.88 kcal/mol. On the other hand, a very different arrangement of the isoxalazine and nicotinamide rings, when compared to the AM1 hydrogen-bonded gas-phase structures, is obtained along the AM1(QM)/CHARMM22(MM) reaction coordinate (see Figure 6). The two rings are set out in a roughly parallel configuration, being the N₁₀-N₁N and N₅-C₄N distances 4.96 and 3.97 Å and 5.28 and 3.96 Å at the reactant and product minima, respectively. As the AM1 model in the gas phase has been shown to fail for describing stacking interactions (see Supporting Information), this geometrical arrangement (in better agreement with crystallographic data, see section 5.4) must be attributed to both polarization and steric effects of the QM/MM environment.

As explained previously, the MPWB1K hybrid functional has been selected in this study to correct AM1 potential energies along the hydride-transfer reaction path in the enzyme within a single-point dual-level scheme (see next section). For this purpose, AM1 and MPWB1K single-point energy calculations were carried out on a subset of QM atoms (that has been called QM-c) of the entire QM region all along the AM1/CHARMM22 reaction path generated by z_{AM1}^{RP} . Note that the QM-c set of atoms corresponds to the gas-phase model used in the previous section (see Figure 5) to carry out gas-phase comparisons. The obtained low level, $V_{QM-c}^{AM1}(z_{AM1}^{RP})$, and high level, $V_{QM-c}^{MPWB1K}(z_{AM1}^{RP})$, single-point potential energy curves are plotted for comparison purposes in Figure 7.

5.3. Potential of Mean Force. The next stage is the calculation of the PMF along the reaction coordinate z , which

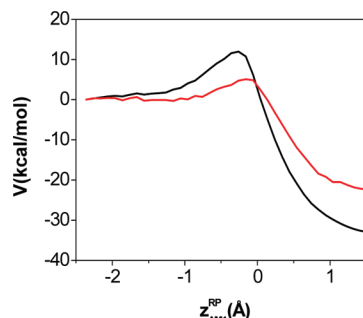


Figure 7. Low level, $V_{QM-c}^{AM1}(z_{AM1}^{RP})$ (in black) and high level, $V_{QM-c}^{MPWB1K}(z_{AM1}^{RP})$ (in red) single-point potential energy curves as a function of z_{AM1}^{RP} .

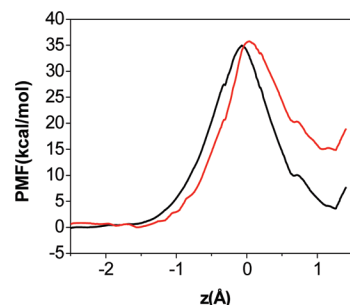


Figure 8. Classical mechanical PMF. $W^{AM1-CM}(z)$ (black) uses AM1 as the QM method of the QM/MM calculations. $W^{DL-CM}(z)$ (red) is the dual-level PMF based on a MPWB1K energy correction.

is defined geometrically as the difference between the N₅-H distance that breaks and the H-C₄N distance that forms. The classical mechanical PMF, $W^{CM}(z)$, is displayed in Figure 8. In this figure two curves are presented. The first one, $W^{AM1-CM}(z)$, has been obtained by using the semiempirical AM1 method as the QM method of the QM/MM calculations. However, as said before, AM1 can fail to describe some interactions, particularly π stacking interactions, which are relevant in the present system. Thus we have applied a dual-level approach to correct the deficiencies of the AM1 energies. This strategy is akin to the ONIOM model^{67,68} and has been already successfully used in several QM/MM simulations. In particular, we have applied the method proposed by Wong and Gao.⁶⁹ From the single-point AM1 and MPWB1K energy calculations leading, respectively, to the potential energy curves $V_{QM-c}^{AM1}(z_{AM1}^{RP})$ and $V_{QM-c}^{MPWB1K}(z_{AM1}^{RP})$ shown in Figure 7, the dual-level classical mechanical PMF, the second curve displayed in Figure 8, is obtained as

$$W^{DL-CM}(z) = W^{AM1-CM}(z) + [V_{QM-c}^{MPWB1K}(z_{AM1}^{RP}) - V_{QM-c}^{AM1}(z_{AM1}^{RP})] \quad (7)$$

where the reaction coordinate z_{AM1}^{RP} emphasizes that the correction term (in square brackets) is made along the reaction path in the enzyme at the AM1/CHARMM22 level (see Figure 6).

$W^{AM1-CM}(z)$ turns out to be quite similar to the AM1/CHARMM22 potential energy profile. This indicates that the effect of the thermal and entropic contributions is small. The reactant, transition state and product are located at the values $z_R^{AM1-CM} = -2.44$ Å (the curve is very flat in this region), $z_{\ddagger}^{AM1-CM} = -0.07$ Å, and $z_P^{AM1-CM} = 1.26$ Å, respectively. The PMF difference between the transition state and the reactant is 34.91 kcal/mol, whereas this difference between the transition state and the product is 31.28 kcal/mol. Then, in terms of PMF, the reaction HT-1 is somewhat endoergic (3.63 kcal/mol). The

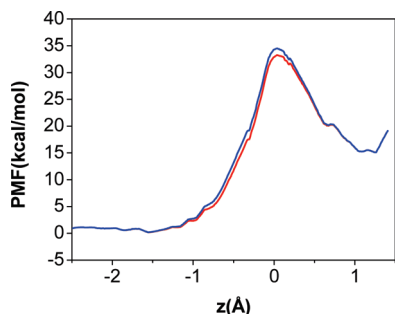


Figure 9. Undeuterated (red) and deuterated (blue) quasiclassical PMF.

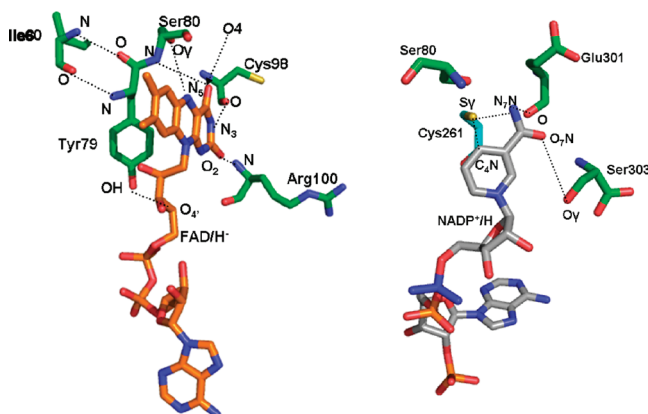


Figure 10. Main interactions in the active site. The corresponding distances are given in Table 1.

introduction of the MPWB1K energy correction only changes significantly the endergonicity of the reaction. Now the reactant, transition state and product corresponding to $W^{\text{DL-CM}}(z)$ are located at the values $z_{\text{R}}^{\text{DL-CM}} = -1.56$ Å, $z_{\text{TS}}^{\text{DL-CM}} = 0.04$ Å, and $z_{\text{P}}^{\text{DL-CM}} = 1.26$ Å, respectively. The PMF difference between the transition state and the reactant is 35.79 kcal/mol. The fact that the AM1 and MPWB1K potential energy curves in Figure 7 cross at $z_{\text{AM1}}^{\text{RP}} = 0$ causes that $W^{\text{DL-CM}}(z)$ is below $W^{\text{AM1-CM}}(z)$ for $z < 0$, but above for $z > 0$, in such a way that the MPWB1K energy correction slightly delays the location of the maximum, keeping practically unchanged its free energy height with respect to the reactant. However, the PMF difference between the transition state and the product, and the endergonicity have been noticeably reduced and augmented to 20.90 and 14.89 kcal/mol, respectively. From hereafter we will use $W^{\text{DL-CM}}(z)$ as $W^{\text{CM}}(z)$ in eqs 1–3.

The quantal vibrational correction corresponding to the vibrational modes orthogonal to the reaction coordinate $\Delta W_{\text{vib}}(z)$ has been calculated and added to $W^{\text{CM}}(z)$ to give the quasiclassical PMF $W^{\text{QC}}(z)$, which is displayed in Figure 9. Note that this $W^{\text{QC}}(z)$ already includes the MPWB1K energy correction. For the undeuterated case the vibrational correction does not change the location of reactant ($z_{\text{R}}^{\text{QC}} = -1.56$ Å) and product ($z_{\text{P}}^{\text{QC}} = 1.26$ Å) and produces an insignificant displacement of the transition state ($z_{\text{TS}}^{\text{QC}} = 0.05$ Å), which now appears 33.29 and 18.60 kcal/mol above reactant and product, respectively, thus leading to an endergonicity of 14.69 kcal/mol. It is worth noting that the vibrational contribution lowers the relative free energy of the transition state around 2.5 kcal/mol.

5.4. Structural Analysis. At this point we can do a structural analysis of the main interactions (marked in Figure 10) in the active site and follow their evolution along the reaction path. Table 1 shows the calculated average distances between the FAD/H[−] cofactor or the NADP⁺/H coenzyme and several close

residues, along with some distances between Tyr79 and Ile60 (these residues stack against the flavin *si* face that is not involved in coenzyme contact). The values corresponding to the reactant, transition state, and product have been obtained by averaging over the set of configurations generated within the ranges of $z = z_{\text{R}}^{\text{QC}} \pm 0.05$ Å, $z = z_{\text{TS}}^{\text{QC}} \pm 0.025$ Å, and $z = z_{\text{P}}^{\text{QC}} \pm 0.02$ Å. For the sake of comparison, the corresponding values obtained by X-ray crystallography of the Tyr303Ser FNR_{ox}:NADP⁺ complex in *Anabaena* are also given in the third column of Table 1.

The agreement between the X-ray distances and the ones coming from our simulation at the reactant region is remarkable, with some deviations for the interactions with NADP⁺. These deviations are a consequence of some rotation of the amide group attached to the nicotinamide ring due to the thermal motion in the umbrella sampling simulation. This rotation approaches the N₇N atom to both Glu301 and Cys261, while the O₇N atom goes away from Ser303 and Cys261 separates from the C₄N atom of the nicotinamide ring. Along the reaction path the most notorious change in Table 1 corresponds to the progressive separation of Cys261 from the C₄N atom, as this one is receiving the transferring hydride. Simultaneously, Ser80 goes away from the N₅ atom of FAD/H[−], and Glu301 and the N₇N atom come a bit closer. The rest of distances are maintained roughly invariant in going from reactant to product.

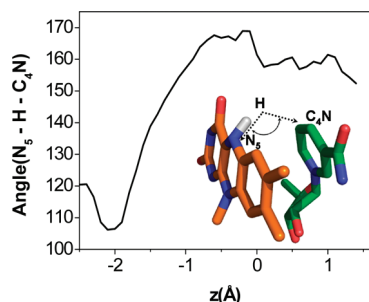
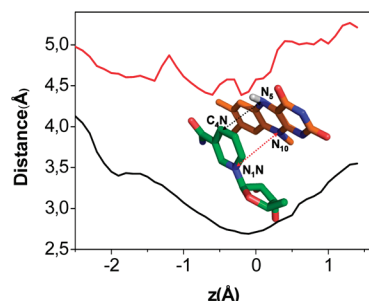
As mentioned above, the proximity between the isoalloxazine and nicotinamide rings seems to be very suitable to produce an easy hydride transfer, because the distance from the N₅ hydride donor to the C₄N hydride acceptor corresponding to the reaction HT-1 is only of 3.4 Å in the crystallographic structure of *Anabaena* Tyr303Ser FNR:NADP⁺ complex. In spite of that, the quasiclassical PMF shown in Figure 9 indicates that the hydride transfer costs a lot of free energy, most of it coming from the potential energy barrier.

To get a deeper insight in how the hydride transfer happens, we have calculated the evolution along the reaction coordinate of the N₅–hydride–C₄N angle (see Figure 11), and the N₅–C₄N and N₁₀–N₁N distances (see Figure 12). N₁₀ and N₁N are the opposite atoms to N₅ and C₄N in their respective rings. The comparison between the two distances allows us to envisage the degree of parallelism between the isoalloxazine and the nicotinamide rings. Those three geometric parameters have been calculated by averaging over the set of configurations generated within each bin. At $z = z_{\text{R}}^{\text{QC}}$ the angle is roughly 135°, very far from the colinearity, in such a way that the hydride shift is quite little efficient. This angle is a consequence of the π stacking interaction between the isoalloxazine and nicotinamide rings that favors a vertical stacked configuration of both groups. In effect, at the reactant bin the N₅–C₄N and N₁₀–N₁N distances are 3.4 and 4.6 Å, respectively, just the values found in the crystallographic structure where the two rings align with an angle of $\sim 30^\circ$. The two rings are not parallel probably due to the steric hindrance derived from the two long chains attached to the N₁₀ atom (an adenine dinucleotide) and the N₁N atom (an adenine dinucleotide phosphate). To make the hydride transfer easier, the N₅–hydride–C₄N angle has to approach to 180°, and the hydride donor and acceptor atoms have to come closer. This is what actually happens from the reactant region to $z = z_{\text{TS}}^{\text{QC}}$, where the angle is already about 160° (see Figure 11), and the N₅–C₄N and N₁₀–N₁N distances are 2.75 and 4.6 Å, respectively (see Figure 12). Note that the approach of the two rings occurs just by the side free of the attached chains, in such a way that the angle between them increases. All these geometric deformations, including a partial loss of the π stacking

TABLE 1: X-ray and Calculated Average Distances (Å) between the Cofactor FAD/H⁻ or the NADP⁺/H and Several Close Residues, along with Some Distances between Tyr79 and Ile60^a

atom1	atom2	X-ray	R	TS	P
N-Arg100	O ₂ -FAD/H ⁻	3.0	2.99 ± 0.01	3.14 ± 0.02	3.19 ± 0.02
OH-Tyr79	O ₄ -FAD/H ⁻	2.9	2.89 ± 0.01	2.84 ± 0.02	2.85 ± 0.01
Oγ-Ser80	N ₅ -FAD/H ⁻	3.3	3.55 ± 0.00	3.60 ± 0.03	3.80 ± 0.04
N-Ser80	O ₄ -FAD/H ⁻	3.3	3.66 ± 0.01	3.43 ± 0.01	3.70 ± 0.01
O-Cys98	N ₃ -FAD/H ⁻	2.9	3.05 ± 0.00	3.03 ± 0.01	3.02 ± 0.02
O-Glu301	N ₇ N-NADP ⁺ /H	4.3	3.78 ± 0.03	3.70 ± 0.06	3.42 ± 0.03
Sγ-Cys261	N ₇ N-NADP ⁺ /H	5.0	3.71 ± 0.01	3.52 ± 0.04	3.66 ± 0.01
Sγ-Cys261	C ₄ N-NADP ⁺ /H	3.3	3.71 ± 0.01	3.95 ± 0.02	4.28 ± 0.02
Oγ-Ser303	O ₇ N-NADP ⁺ /H	3.0	4.13 ± 0.01	4.23 ± 0.03	4.14 ± 0.04
O-Tyr79	N-Ile60	3.1	2.92 ± 0.01	2.97 ± 0.01	2.91 ± 0.01
N-Tyr79	O-Ile60	3.0	2.88 ± 0.00	2.89 ± 0.02	2.89 ± 0.02

^a The standard deviations of the values in our simulation are also included. R, TS, and P stand for the reactant, transition state, and product, respectively. See Figure 10 for the labels of atoms and residues.

**Figure 11.** Evolution along the reaction coordinate of the N₅-hydride-C₄N angle (in degrees).**Figure 12.** Evolution along the reaction coordinate of the N₅-C₄N (black) and N₁₀-N₁N (red) distances.

interaction, involve a penalty that increases the free energy cost of the transition state. At the product region, where the hydride transfer has already happened and both flavin and NADPH are neutral, both rings become somewhat more separated and clearly less parallel than in the reactant region, which also makes a more collinear disposition of the hydride between the donor and acceptor atoms possible.

5.5. Rate Constants. The classical mechanical activation free energy ($\Delta G_{\text{act}}^{\text{CM}}(z)$) and the quassiclassical activation free energy ($\Delta G_{\text{act}}^{\text{QC}}(z)$) profiles have been obtained from the respective PMFs through eqs 1 and 3. $\Delta G_{\text{act}}^{\text{QC}}(z)$ includes the quantal correction corresponding to the reaction coordinate and the vibrational modes orthogonal to it. Their maximum values, the free energy barriers, $\Delta G_{\text{act}}^{\text{CM}}(z_{\text{QC}}^{\text{CM}})$ and $\Delta G_{\text{act}}^{\text{QC}}(z_{\text{QC}}^{\text{QC}})$ are given in Table 2. It can be seen that the introduction of the quantal corrections clearly reduces the free energy barriers. Very interestingly, the quassiclassical free energy barrier for the reaction HT-1 is almost twice as big as the corresponding value for the reverse reaction, HT.

According to eq 5 the EA-VTST/MT rate constant also depends on the average net transmission coefficient γ , which includes the dynamical recrossing and the quantum effects on

the reaction coordinate, that is, tunneling and nonclassical reflection. So we have chosen 8 configurations in the bin corresponding to the quassiclassical transition state ($z = z_{\text{QC}}^{\text{QC}}$) and for each of them we have located a saddle point under the SSZ approximation. Then, the MEPs going downhill through the primary zone from each saddle point were built at the AM1/CHARMM22 level. The potential energy of each MEP was corrected from single-point AM1 and MPWB1K energy calculations on a QM-c system (see definition in Figure 5) with geometries corresponding to the points generated along the MEP. Thus a dual-level correction analogous to the one previously done for the classical mechanical PMF is now made for each MEP. However, in this case an interpolation of the correction according to the ISPE method has been done.⁷⁰ These dual-level MEPs are used to determine the individual quassiclassical transmission factors (Γ_i) and the semiclassical transmission coefficients (κ_i). The average values of the transmission factors over the set of the 8 configurations are given in Table 2. The range of values of the transmission factors across the ensemble of configurations chosen are given in the Supporting Information (Table S3). $\langle \Gamma_i \rangle$ is nearly 1 with a negligible standard deviation, which indicates the absence of significant fluctuations among the different configurations. On the contrary, $\langle \kappa_i \rangle$ is a very remarkable contribution to the rate constant. Its standard deviation is also quite significant, so indicating the heterogeneity of the canonical ensemble of configurations corresponding to the transition state in what refers to tunneling. It is clear that the hydride transfer involves a high degree of quantum mechanical tunneling. Indeed, in this case the net transmission coefficient, γ , practically matches the value of $\langle \kappa_i \rangle$.

Including all the above contributions we have obtained the rate constants and the theoretical estimate of the phenomenological free energies of activation at 279 K (see the last two columns in Table 2). Our theoretical analysis indicates that for this mutant the physiological FNR reaction HT-1 has a completely negligible reaction rate ($k_{\text{HT-1}}^{\text{EA-VTST/MT}}$ is $2.24 \times 10^{-10} \text{ s}^{-1}$) with an associated phenomenological free energy of activation of 28.64 kcal/mol. This result agrees with our stopped-flow kinetic measurements showing that the hydride transfer from Tyr303Ser FNR_{rd} to NADP⁺ hardly occurs. That is, the mutant Tyr303Ser FNR is unable to retain the physiological main role of the WT enzyme. Conversely, the reverse reaction, HT, does happen, with a reaction rate constant of 92.76 s^{-1} ($k_{\text{HT}}^{\text{EA-VTST/MT}}$), a value whose agreement with our stopped-flow kinetic measurements ($k_{\text{HT}} = 190 \text{ s}^{-1}$ at 279 K) is very good taking into account the huge complexity of the system studied and the exponential dependence of the rate constant on the free energy barrier (note that at 279 K and with the value of γ for

TABLE 2: Classical and Quassiclassical Free Energy Barriers (kcal/mol), Average Transmission Coefficients (Including the Standard Deviations), Rate Constants (s⁻¹), and Phenomenological Free Energies of Activation (kcal/mol) at 279 K^a

	$\Delta G_{\text{act}}^{\text{CM}}(\epsilon_{*}^{\text{CM}})$	$\Delta G_{\text{act}}^{\text{QC}}(\epsilon_{*}^{\text{QC}})$	$\langle \Gamma_i \rangle$	$\langle \kappa_i \rangle$	γ	$k^{\text{EA-VTST/MT}}$	$\Delta G_{\text{act}}^{\text{EA-VTST/MT}}$
HT-1	35.04	31.87	0.998 ± 0.003	335.70 ± 142.79	334.82 ± 142.44	2.24 × 10 ⁻¹⁰	28.64
HT	20.08	17.02	0.998 ± 0.003	335.70 ± 142.79	334.82 ± 142.44	92.76	13.80
DT-1	35.00	32.67	0.999 ± 0.00	56.37 ± 22.90	56.29 ± 22.84	8.87 × 10 ⁻¹²	30.43
DT	20.08	17.85	0.999 ± 0.00	56.37 ± 22.90	56.29 ± 22.84	3.52	15.61

^a HT-1 and HT stand for the undeuterated direct and reverse reactions, respectively. DT-1 and DT denote the deuterated direct and reverse reactions, respectively.

this reaction, a change as small as ± 0.5 kcal/mol in the value of the quassiclassical free energy barrier brings the corresponding rate constant from 36 to 220 s⁻¹). Therefore, in agreement with the experimental results the physiological process does not occur for Tyr303Ser, while hydride transfer from NADPH is slightly slower than in the WT enzyme.

Due to tunneling, the phenomenological free energy of activation for the reverse reaction is 13.80 kcal/mol, more than 3 kcal/mol lower than the corresponding quassiclassical free energy barrier. This very significant contribution of tunneling was already anticipated as the explanation of the experimental KIE features described in the section 4.3. There would be less tunneling contribution at higher temperatures through a static potential energy barrier, which would tend to lower the KIE. However, if the protein is flexible enough in such a way that thermal fluctuations are able to compress the hydride donor–acceptor coordinate (gating), the potential energy barrier becomes narrower at higher temperatures, so compensating the above effect and causing an essentially temperature-independent KIE: It is a vibration-driven tunneling.^{56,57} This is what occurs in this reaction. It has been already shown in section 5.4 that the hydride donor (N₅) and the hydride acceptor (C₄N) have to come closer to permit the hydride transfer. So the reduction of the potential energy barrier width as the temperature increases reinforces the role of tunneling.

5.6. Primary Kinetic Isotope Effect. We have also calculated the primary kinetic isotope effect (KIE) corresponding to the substitution of the protium being transferred by a deuterium. Now, to obtain the quassiclassical PMF (see Figure 9) and the activation free energy profiles for the deuterated system, we have taken into account that the frequencies used to calculate the classical mechanical vibrational free energy of the reactant that accounts for the reaction coordinate, and the quantal correction corresponding to the reaction coordinate and the vibrational modes orthogonal to it, depend on the masses. All the results corresponding to the deuterated system are also given in Table 2. The changes in the classical mechanical free energy barriers are negligible, but the two quassiclassical free energy barriers grow about 1 kcal/mol for the deuterated case, causing the vibrational contribution to the KIE.

Starting from the 8 saddle points located under the SSZ approximation, we have rebuilt the new AM1/CHARMM22 MEPs for the deuterated case, and the corresponding dual-level corrected MEPs, which are used to determine the individual quassiclassical transmission factors (Γ_i) and the semiclassical transmission coefficients (κ_i) (Table S3, Supporting Information). Again $\langle \Gamma_i \rangle$ is nearly 1, showing the lack of dynamical recrossing. As expected, the deuteration noticeably reduces the semiclassical transmission coefficient average and its standard deviation, although tunneling is still significant for the deuteride transfer. Again, the net transmission coefficient γ practically matches the value of $\langle \kappa_i \rangle$.

As for the reaction rate constants, the deuterated reaction DT-1 would be even slower than the HT-1, but this result is

not relevant taking into account the fact that we have already shown that Tyr303Ser FNR_{rd} is unable in practice to transfer a hydride (or deuteride) to NADP⁺. More interesting is the calculated value of the rate constant for the reverse deuterated reaction DT ($k_{\text{DT}}^{\text{EA-VTST/MT}}$), which turns out to be 3.52 s⁻¹, with a phenomenological free energy of activation of 15.61 kcal/mol, nearly 2 kcal/mol higher than for the undeuterated reaction HT. Then a KIE of 26.33 is predicted by our calculations, arising from both the vibrational and tunneling contributions to the KIE. This value is somewhat higher than the experimental value of 11.6 we have obtained by stopped-flow kinetic measurements. This discrepancy is not very significant taking into account the high exponential dependence of the rate constants on the theoretical free energy barriers, as commented above. The effect of any small error is amplified by the very important tunneling contribution introduced through the γ factor. Interestingly, in a very recent theoretical work⁷¹ about the hydride-transfer reaction from NADH to flavin mononucleotide in morphinone reductase (an analogous reaction, also with a very remarkable tunneling contribution), a calculated primary KIE as big as 15.4 (also corresponding to deuteration of NADH) was found, in comparison with the experimental value of 4.6.

6. Conclusions

In this paper we present a combined experimental/theoretical study of the hydride-transfer processes between *Anabaena* Tyr303Ser FNR_{rd}/FNR_{ox} and NADP⁺/H. The stopped-flow pre-steady-state kinetic measurements have shown that, in contrast to that observed for WT FNR, the physiological hydride transfer from Tyr303Ser FNR_{rd} to NADP⁺ is not possible. However, the reverse reaction, the hydride transfer from NADPH to Tyr303Ser FNR_{ox}, does occur, being only slightly slower than for WT FNR, and taking place in a larger extension. We have also performed a fully microscopic simulation of this hydride transfer in the FNR mutant bound to the NADP⁺ coenzyme, with the corresponding solvation shell of water molecules. We have used a dual level QM/MM hybrid approach to describe the potential energy surface of the whole system, and the ensemble-averaged variational transition-state theory with multidimensional tunneling to calculate the rate constant and the corresponding H/D primary kinetic isotope effect. The theoretical results confirm that only the reverse reaction occurs, the experimental and theoretical reverse reaction rate constants being in very good accordance, taking into account the number of uncertainties inherent to both methods. This very good agreement between results coming from extremely opposite ways to face the problem guarantees their goodness.

One advantage of the theoretical approach is that it is able to provide subtle structural details of the mechanism that could be unavailable with experimental techniques. At the reactant region (Tyr303Ser FNR_{rd}:NADP⁺) the N₅–C₄N distance might be compatible with the hydride transferred, but the angle formed between the N₅ hydride donor atom, the hydride to be

transferred, and the hydride C₄N acceptor atom (N₅–hydride–C₄N) is very far from collinearity, and therefore, the hydride shift is quite inefficient. This angle is a consequence of the π stacking interaction between the isoalloxazine and nicotinamide rings that favors a vertical stacked configuration of both groups. In going from the reactant region to the transition-state region the N₅–hydride–C₄N angle approaches 180° to make the hydride transfer easier, and the hydride donor and acceptor atoms come closer. Since the width of the hydride-transfer reaction path is small, the hydride transfer involves an important degree of quantum mechanical tunneling. All those geometric deformations, including a partial loss of the π stacking interaction, involve a large free energy penalty to reach the transition state, so leading to an undetectable direct reaction and a slow reverse reaction.

The difference between the direct and the reverse reaction rates comes from the important positive reaction free energy (the reactant is ~ 15 kcal/mol more stable than the product). Such a difference must be due to an important stabilization of the ionic pair FADH[−]:NADP⁺ by the close contact between both molecules when surrounded by the environment of the enzyme, versus the situation corresponding to the product, where, after the hydride transfer, the two moieties are neutral. Therefore, in spite of the apparent favorable closeness between the isoalloxazine and the nicotinamide rings to produce the hydride transfer, the mutant Tyr303Ser FNR is unable to retain the physiological main role of the WT enzyme. It seems clear that any factor able to distort the formation of that close contact ionic pair would destabilize the reactant, so increasing the rate constant of the direct reaction. Very interestingly, the affinity for the coenzyme in the WT FNR is much lower than in the mutant Tyr303Ser FNR (see section 4.2), this fact being consistent with the feasibility of the direct hydride transfer corresponding to the physiological main role of the enzyme. Could this lower affinity in the WT FNR be attributed to the presence of Tyr303 distorting in some way the formation of a close contact ionic pair as stable as in the Tyr303Ser mutant, with the corresponding thermodynamic and kinetic consequences? Unfortunately, this hypothesis cannot yet be easily verified because no crystallographic structure exists for the WT FNR_{rd}-NADP⁺ CTC-2 or FNR_{ox}-NADPH CTC-1, the reactant and product of the HT-1 reaction, showing the position occupied by Tyr303. Therefore, the Tyr303 and NADP⁺ allocations ready for either reaction, HT-1 or HT, in the active site of the WT FNR still remain unknown. Theoretical work to address this point and to study the corresponding hydride-transfer processes is now under progress in our laboratories.

Acknowledgment. This work has been supported by Ministerio de Ciencia e Innovación, Spain (Grants BIO2007-65890-C02-01 to M.M. and CTQ2008-02403/BQU to J.M.L.) and by CONSI+D, DGA (Grant PM062/2007 to M.M.). I.L. is the recipient of a JAE-CSIC fellowship associated to the Instituto Química-Física Rocasolano. We thank A. Sanchez-Azqueta for her collaboration in early stages of the stopped-flow measurements.

Supporting Information Available: Complete refs 26 and 35. Scheme for the WT and Tyr303Ser processes. Gas-phase calculations. Range of values of the transmission factors. This material is available free of charge via Internet at <http://pubs.acs.org>.

References and Notes

(1) Arakaki, A. K.; Ceccarelli, E. A.; Carrillo, N. *FASEB J.* **1997**, *11*, 133–140.

- (2) Carrillo, N.; Ceccarelli, E. A. *Eur. J. Biochem.* **2003**, *270*, 1900–1915.
- (3) Ceccarelli, E. A.; Arakaki, A. K.; Cortez, N.; Carrillo, N. *Biochim. Biophys. Acta* **2004**, *1698*, 155–165.
- (4) Medina, M.; Gómez-Moreno, C. *Photosynth. Res.* **2004**, *79*, 113–131.
- (5) Medina, M. *FEBS J.* **2009**, *276*, 3942–3958.
- (6) Correll, C. C.; Ludwig, M. L.; Bruns, C. M.; Karplus, P. A. *Protein Sci.* **1993**, *2*, 2112–2133.
- (7) Wolthers, K. R.; Scrutton, N. S. *Biochemistry* **2007**, *46*, 6696–6709.
- (8) Karplus, P. A.; Bruns, C. M. *J. Bioenerg. Biomembr.* **1994**, *26*, 89–99.
- (9) Serre, L.; Vellieux, F. M.; Medina, M.; Gomez-Moreno, C.; Fontecilla-Camps, J. C.; Frey, M. J. *Mol. Biol.* **1996**, *263*, 20–39.
- (10) Hermoso, J. A.; Mayoral, T.; Faro, M.; Gomez-Moreno, C.; Sanz-Aparicio, J.; Medina, M. *J. Mol. Biol.* **2002**, *319*, 1133–1142.
- (11) Batie, C. J.; Kamin, H. J. *Biol. Chem.* **1984**, *259*, 11976–11985.
- (12) Velazquez-Campoy, A.; Goñi, G.; Peregrina, J. R.; Medina, M. *Biophys. J.* **2006**, *91*, 1887–1904.
- (13) Peregrina, J. R.; Herguedas, B.; Hermoso, J. A.; Martínez-Júlvez, M.; Medina, M. *Biochemistry* **2009**, *48*, 3109–3119.
- (14) Tejero, J.; Pérez-Dorado, I.; Maya, C.; Martínez-Júlvez, M.; Sanz-Aparicio, J.; Gómez-Moreno, C.; Hermoso, J. A.; Medina, M. *Biochemistry* **2005**, *44*, 13477–13490.
- (15) Paladini, D. H.; Musumeci, M. A.; Carrillo, N.; Ceccarelli, E. A. *Biochemistry* **2009**, *48*, 5760–5768.
- (16) Piubelli, L.; Aliverti, A.; Arakaki, A. K.; Carrillo, N.; Ceccarelli, E. A.; Karplus, P. A.; Zanetti, G. *J. Biol. Chem.* **2000**, *275*, 10472–10476.
- (17) Deng, Z.; Aliverti, A.; Zanetti, G.; Arakaki, A. K.; Ottado, J.; Orellano, E. G.; Calcaterra, N. B.; Ceccarelli, E. A.; Carrillo, N.; Karplus, P. A. *Nat. Struct. Biol.* **1999**, *6*, 847–853.
- (18) Tejero, J.; Peregrina, J. R.; Martínez-Júlvez, M.; Gutiérrez, A.; Gómez-Moreno, C.; Scrutton, N. S.; Medina, M. *Arch. Biochem. Biophys.* **2007**, *459*, 79–90.
- (19) Nogués, I.; Tejero, J.; Hurley, J. K.; Paladini, D.; Frago, S.; Tollin, G.; Mayhew, S. G.; Gómez-Moreno, C.; Ceccarelli, E. A.; Carrillo, N.; Medina, M. *Biochemistry* **2004**, *43*, 6127–6137.
- (20) Medina, M.; Martínez-Júlvez, M.; Hurley, J. K.; Tollin, G.; Gomez-Moreno, C. *Biochemistry* **1998**, *37*, 2715–2728.
- (21) Pollock, V. V.; Barber, M. J. *Biochemistry* **2001**, *40*, 1430–1440.
- (22) Field, M. J.; Bash, P. A.; Karplus, M. *J. Comput. Chem.* **1990**, *11*, 700–733.
- (23) Gao, J., Methods and Applications of Combined Quantum Mechanical and Molecular Mechanical Potentials. In *Reviews in Computational Chemistry*; Lipkowitz, K. B.; Boyd, D. B., Eds.; VCH: New York, 1995; Vol. 7, pp 119–185.
- (24) Gao, J.; Amara, P.; Alhambra, C.; Field, M. J. *J. Phys. Chem.* **1998**, *102*, 4714–4721.
- (25) Dewar, M. J. S.; Zoebisch, E. G.; Healy, E. F.; Stewart, J. J. P. *J. Am. Chem. Soc.* **1985**, *107*, 3902–3909.
- (26) Frisch, M. J.; et al. *GAUSSIAN03*, Gaussian: Wallingford, CT, 2004.
- (27) Zhao, Y.; Truhlar, D. G. *J. Phys. Chem. A* **2004**, *108*, 6908–6918.
- (28) Becke, A. D. *J. Chem. Phys.* **1993**, *98*, 5648–5652.
- (29) Lee, C.; Yang, W.; Parr, R. G. *Phys. Rev. B* **1988**, *37*, 785–789.
- (30) Brooks, B.; Bruccoleri, R.; Olafson, B.; States, D.; Swaminathan, S.; Karplus, M. *J. Comput. Chem.* **1983**, *4*, 187–217.
- (31) Li, H.; Robertson, A. D.; Jensen, J. H. *Proteins* **2005**, *61*, 704–721.
- (32) Bas, D. C.; Rogers, D. M.; Jensen, J. H. *Proteins* **2008**, *73*, 765–783.
- (33) Dolinsky, T. J.; Czodrowski, P.; Li, H.; Nielsen, J. E.; Jensen, J. H.; Klebe, G.; N. A. B. *Nucleic Acids Res.* **2007**, *35*, 522–525.
- (34) Dolinsky, T. J.; Nielsen, J. E.; McCammon, J. A.; Baker, N. A. *Nucleic Acids Res.* **2004**, *32*, 665–667.
- (35) MacKerell, A. D. J.; Bashford, D.; Bellott, M.; Dunbrack, R. L. J.; Evanseck, J. D.; Field, M. J.; Fischer, S.; Gao, J.; Guo, H.; Ha, S.; Joseph-McCarthy, D.; Kuchnir, L.; Kuczera, K.; Lau, F. T. K.; Mattos, C.; Michnick, S.; Ngo, T.; Nguyen, D. T.; Prodhom, B.; Reiher, W. E., III; Roux, B.; Schlenkrich, M.; Smith, J. C.; Stote, R. G.; Straub, J.; Watanabe, M.; Wiórkiewicz-Kuczera, J.; Yin, D.; Karplus, M. *J. Phys. Chem. B* **1998**, *102*, 3586–3616.
- (36) Jorgensen, W. L.; Chandrasekhar, J.; Madura, J. D.; Impey, R. W.; Klein, M. L. *J. Chem. Phys.* **1983**, *79*, 926–935.
- (37) Bayly, C. I.; Cieplak, P.; Cornell, W. D.; Kollman, P. A. *J. Phys. Chem.* **1993**, *97*, 10269–10280.
- (38) Cornell, W. D.; Cieplak, P.; Bayly, C. I.; Kollman, P. A. *J. Am. Chem. Soc.* **1993**, *115*, 9620–9631.
- (39) Ulrich, E.; Lalith, P.; Max, L. B.; Tom, D.; Hsing, L.; Lee, G. P. *J. Chem. Phys.* **1995**, *103*, 8577–8593.
- (40) Hockney, R. W. *Meth. Comput. Phys.* **1970**, *9*, 136–211.
- (41) Ryckaert, J. P.; Ciccotti, G.; Berendsen, H. J. C. *J. Comput. Phys.* **1977**, *23*, 327–341.

- (42) Kumar, S.; Rosenberg, J. M.; Bouzida, D.; Swendsen, R. H.; Kollman, P. A. *J. Comput. Chem.* **1992**, *13*, 1011–1021.
- (43) Rajamani, R.; Naidoo, K. J.; Gao, J. *J. Comput. Chem.* **2003**, *24*, 1775–1781.
- (44) Boczek, E. M.; Brooks, C. L., III. *J. Phys. Chem.* **1993**, *97*, 4509–4513.
- (45) Garcia-Viloca, M.; Alhambra, C.; Corchado, J. C.; Sánchez, M. L. S.; Villa, J.; Gao, J.; Truhlar, D. G. *CHARMMRATE*, 2.0; University of Minnesota: Minneapolis, 2002.
- (46) Alhambra, C.; Corchado, J.; Sanchez, M. L.; Garcia-Viloca, M.; Gao, J.; Truhlar, D. G. *J. Phys. Chem. B* **2001**, *105*, 11326–11340.
- (47) Garcia-Viloca, M.; Alhambra, C.; Truhlar, D. G.; Gao, J. *J. Chem. Phys.* **2001**, *114*, 9953–9958.
- (48) Garcia-Viloca, M.; Alhambra, C.; Truhlar, D. G.; Gao, J. *J. Comput. Chem.* **2003**, *24*, 177–190.
- (49) Marcus, R. A. *J. Chem. Phys.* **1968**, *49*, 2610–2616.
- (50) Shavitt, I. *J. Chem. Phys.* **1968**, *49*, 4048–4056.
- (51) Truhlar, D. G.; Kuppermann, A. *J. Am. Chem. Soc.* **1971**, *93*, 1840–1851.
- (52) Liu, Y. P.; Lynch, G. C.; Truong, T. N.; Lu, D. H.; Truhlar, D. G.; Garrett, B. C. *J. Am. Chem. Soc.* **1993**, *115*, 2408–2415.
- (53) Truhlar, D. G.; Gao, J.; Garcia-Viloca, M.; Alhambra, C.; Corchado, J.; Sanchez, M. L.; Poulsen, T. D. *Int. J. Quantum Chem.* **2004**, *100*, 1136–1152.
- (54) Batie, C. J.; Kamin, H. *J. Biol. Chem.* **1986**, *261*, 11214–11223.
- (55) Massey, V.; Matthews, R. G.; Foust, G. P.; Howell, L. G.; Williams, C. H., Jr.; Zanetti, G.; Ronchi, S. A new intermediate in TPNH-linked flavoproteins in pyridine nucleotide-dependent dehydrogenases. In *Pyridine nucleotide-dependent dehydrogenases*; Sund, H., Ed.; Springer-Verlag: Berlin, 1970; pp 393–411.
- (56) Basran, J.; Sutcliffe, M. J.; Scrutton, N. S. *Biochemistry* **1999**, *38*, 3218–3222.
- (57) Nagel, Z. D.; Klinman, J. P. *Chem. Rev.* **2006**, *106*, 3095–3118.
- (58) Cerny, J.; Hobza, P. *Phys. Chem. Chem. Phys.* **2007**, *9*, 5291–5303.
- (59) Sponer, J.; Riley, K. E.; Hobza, P. *Phys. Chem. Chem. Phys.* **2008**, *19*, 2595–2610.
- (60) Antony, J.; Grimme, S. *Phys. Chem. Chem. Phys.* **2006**, *8*, 5287–5293.
- (61) Grimme, S. *J. Comput. Chem.* **2004**, *25*, 1463–1473.
- (62) Grimme, S. *J. Comput. Chem.* **2006**, *27*, 1787–1799.
- (63) Zhao, Y.; Schultz, N. E.; Truhlar, D. G. *J. Chem. Theory Comput.* **2006**, *2*, 364–382.
- (64) Zhao, Y.; Truhlar, D. G. *Acc. Chem. Res.* **2008**, *41*, 157–167.
- (65) Zhao, Y.; Truhlar, D. G. *Phys. Chem. Chem. Phys.* **2005**, *7*, 2701–2705.
- (66) Dkhissi, A.; Blossey, R. *Chem. Phys. Lett.* **2007**, *439*, 35–39.
- (67) Svensson, M.; Humbel, S.; Froese, R. D. J.; Matsubara, T.; Sieber, S.; Morokuma, K. *J. Phys. Chem.* **1996**, *100*, 19357–19363.
- (68) Dapprich, S.; Komáromi, I.; Byun, K. S.; Morokuma, K.; Frisch, M. J. *THEOCHEM* **1999**, *461–462*, 1–21.
- (69) Wong, K.-Y.; Gao, J. *Biochemistry* **2007**, *46*, 13352–13369.
- (70) Chuang, Y.-Y.; Corchado, J. C.; Truhlar, D. G. *J. Phys. Chem. A* **1999**, *103*, 1140–1149.
- (71) Pang, J.; Hay, S.; Scrutton, N. S.; Sutcliffe, M. J. *J. Am. Chem. Soc.* **2008**, *130*, 7092–7097.

JP912034M